

Learning Neural Free-Energy Functionals with Pair-Correlation Matching

Jacobus Dijkman,^{1,2} Marjolein Dijkstra,³ René van Roij,⁴
Max Welling,² Jan-Willem van de Meent,² and Bernd Ensing^{1,5}

¹*Van 't Hoff Institute for Molecular Sciences, University of Amsterdam, The Netherlands*

²*Informatics Institute, University of Amsterdam, The Netherlands*

³*Debye Institute for Nanomaterials Science, Utrecht University, The Netherlands*

⁴*Institute for Theoretical Physics, Utrecht University, The Netherlands*

⁵*AI4Science Laboratory, University of Amsterdam, The Netherlands*

(Dated: May 15, 2024)

The intrinsic Helmholtz free-energy functional, the centerpiece of classical density functional theory (cDFT), is at best only known approximately for 3D systems. Here we introduce a method for learning a quasi-exact neural-network approximation of this functional by exclusively training on a dataset of radial distribution functions, circumventing the need to sample costly heterogeneous density profiles in a wide variety of external potentials. For a supercritical 3D Lennard-Jones system, we demonstrate that the learned neural free-energy functional accurately predicts planar inhomogeneous density profiles under various complex external potentials obtained from simulations.

Inhomogeneous many-body systems play a profound role in both science and technology, with examples spanning from p-n junctions in semiconducting solid-state devices to phenomena like hydrogen bubbles in electrolyzers, or gas adsorption in porous materials [1–6]. Density functional theory (DFT) is a powerful theoretical framework to describe the thermodynamic equilibrium properties and the structure of such systems, relying solely on the one-body density profile $\rho(\mathbf{r})$ [7]. Classical DFT (cDFT) relies on the existence of an excess free-energy functional $\mathcal{F}_{\text{exc}}[\rho]$, which describes the non-ideal contribution to the total intrinsic free-energy functional $\mathcal{F}[\rho]$ and encompasses the inter-particle interactions. However, the main bottleneck of cDFT is that this functional is in general unknown, and hence, one has to rely on developing accurate approximations for the excess free-energy functionals.

Historically, the field of cDFT has emphasized development of analytical approximations for $\mathcal{F}_{\text{exc}}[\rho]$, often based on thermodynamics and (direct) pair correlations derived from *approximate* closures of the Ornstein-Zernike equation of bulk systems [8]. For instance, the highly successful Fundamental Measure Theory (FMT) for hard spheres is deeply connected to the Percus-Yevick closure [9], and many functionals for systems with soft Van der Waals or Coulombic interactions build on mean-field and mean-spherical approximations [8, 10].

In recent years, there has been a resurgence of cDFT developments facilitated by machine learning (ML) methods, which employ virtually *exact* thermodynamic and structural data obtained from explicit many-body simulations to learn data-driven representations of the excess free-energy functional $\mathcal{F}_{\text{exc}}[\rho]$. In the classical regime, the first machine-learned cDFTs focused on supercritical Lennard-Jones fluids, for which explicit approximate functional forms for $\mathcal{F}_{\text{exc}}[\rho]$ were fitted to density profiles in external fields obtained from simulations, both for 1D [11] and 3D systems in planar geometry [12]. Re-

cent work, once again leveraging simulations of density profiles in a variety of external potentials, has shown that a neural approximation of the functional derivative $\delta\mathcal{F}_{\text{exc}}/\delta\rho$ for hard-sphere systems outperforms FMT [13] in accurately estimating inhomogeneous density profiles.

In this Letter, we introduce a neural free-energy functional that we train using *pair-correlation matching*, a novel optimization objective that matches the Hessian of the neural approximation to pair correlations of particles. We show that pair-correlation matching yields a neural functional that accurately predicts the complete excess free energy for a one-component system of interacting particles. The differentiable nature of this neural functional allows access to, and learning from, various structural and thermodynamic properties by utilizing the first and second functional derivatives of $\mathcal{F}_{\text{exc}}[\rho]$. Unlike previous ML approaches to cDFT [11–14], our neural functional is trained by directly learning pair correlations from radial distribution functions sampled from short simulations of homogeneous bulk systems (illustrated in Fig. 1), rather than inferring from a costly dataset of inhomogeneous densities. We demonstrate that this neural free-energy functional can be applied in the cDFT framework to achieve accurate estimates for inhomogeneous density profiles in external fields without ever having seen any inhomogeneous densities during training. Simultaneously, the neural free-energy functional provides accurate estimates of the excess free energy.

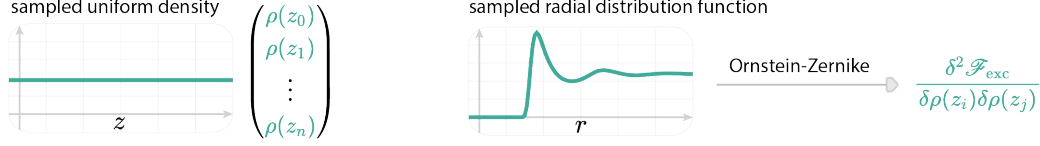
Central to classical DFT is the grand canonical equilibrium density

$$\rho_0(\mathbf{r}) = \frac{1}{\Lambda^3} \exp \left(\beta \mu - \beta \left. \frac{\delta \mathcal{F}_{\text{exc}}[\rho]}{\delta \rho(\mathbf{r})} \right|_{\rho=\rho_0} - \beta V_{\text{ext}}(\mathbf{r}) \right), \quad (1)$$

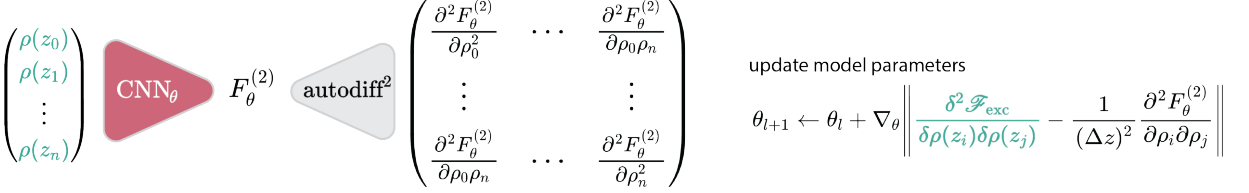
with $\beta = 1/k_B T$, Λ the thermal wavelength, μ the chemical potential and $V_{\text{ext}}(\mathbf{r})$ the external potential. This self-consistency relation can be leveraged to find $\rho_0(\mathbf{r})$ through recursive iteration. Since $\rho_0(\mathbf{r})$ is dependent on $\mathcal{F}_{\text{exc}}[\rho]$ through the first functional derivative

1. Generate training data from MC simulations

— simulation data



2. Train the neural network with pair-correlation matching



3. Classical DFT at fixed $\beta\mu$ and $\beta V^{\text{ext}}(z)$

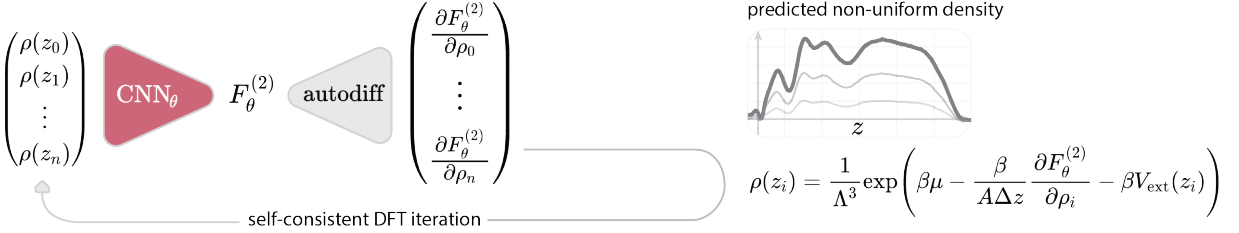


FIG. 1: **1.** Bulk densities in planar geometry $\rho(z_i) = \rho_b$ and radial distribution functions $g(r)$ are sampled from Monte Carlo simulations of homogeneous bulk systems of Lennard-Jones particles. Each $g(r)$ is converted to the second functional derivative of the excess free-energy $\delta^2 \mathcal{F}_{\text{exc}} / \delta \rho(z_i) \delta \rho(z_j)$ by employing the Ornstein-Zernike equation. **2.** Through automatic differentiation (autodiff²), the neural functional $F_\theta^{(2)}$ is optimized to fit the Hessian of the model output with respect to input density profiles to $\delta^2 \mathcal{F}_{\text{exc}} / \delta \rho(z_i) \delta \rho(z_j)$. **3.** The optimized model can then be applied in cDFT to obtain non-uniform equilibrium density profiles through automatic differentiation (autodiff) and the free energy $F_\theta^{(2)}$ for a system of Lennard-Jones particles subjected to arbitrary external potentials.

$\delta \mathcal{F}_{\text{exc}}[\rho] / \delta \rho(\mathbf{r})$, previous approaches to leveraging machine learning for cDFT [11–13] involve training a model to capture $\delta \mathcal{F}_{\text{exc}} / \delta \rho(\mathbf{r})$, which can be derived from sampled inhomogeneous equilibrium density profiles and employing Eq.(1).

In this work, we train a convolutional neural network to directly learn the excess free energy $\mathcal{F}_{\text{exc}}[\rho]$, enabling the straightforward calculation of functional derivatives by (auto-)differentiating the neural functional with respect to its inputs. We focus on 3D systems in a planar geometry, where the excess free energy of a system of area A is a functional of the density $\rho(z)$, which is constant across any plane parallel to the xy -plane, i.e., $\rho(z) = \rho(x, y, z)$ with $\rho(x, y, z) = \rho(x', y', z)$ for all $(x, y), (x', y')$ within the confines of A . We represent the excess free-energy functional $\mathcal{F}_{\text{exc}}[\rho]$ as a neural network $F_\theta^{(2)}(\rho_1, \dots, \rho_n)$, with ρ_i the density at grid point z_i for $i \in \{1, \dots, n\}$, network parameters θ , and where the upper index ‘(2)’ indicates that the neural network is optimized for pair correlations of bulk systems obtained from simulations.

The functional derivative $\delta \mathcal{F}_{\text{exc}} / \delta \rho(z_i)$ is defined as the limit of the partial derivative $\lim_{\Delta z \rightarrow 0} (1/\Delta z) \partial \mathcal{F}_{\text{exc}} / \partial \rho_i$ with $\rho_i = \rho(z_i)$ and Δz the (uniform) grid spacing. We

leverage this relationship by employing automatic differentiation (autodiff) [15, 16] to approximate the first and second functional derivatives of $\mathcal{F}_{\text{exc}}[\rho]$ on a finite grid by $(1/\Delta z) \partial F_\theta^{(2)} / \partial \rho_i$ and $(1/\Delta z)^2 \partial^2 F_\theta^{(2)} / \partial \rho_i \partial \rho_j$, respectively. Here we note that the second functional derivative of $\mathcal{F}_{\text{exc}}[\rho]$ in planar geometry is related to the laterally integrated direct correlation function $\bar{c}_b^{(2)}(|z_i - z_j|)$ through

$$\frac{-\beta}{A} \frac{\delta^2 \mathcal{F}_{\text{exc}}[\rho]}{\delta \rho(z_i) \delta \rho(z_j)} = \bar{c}_b^{(2)}(|z_i - z_j|) \equiv \int_{|z_i - z_j|}^{\infty} dr 2\pi r c_b^{(2)}(r), \quad (2)$$

where the direct correlation function $c_b^{(2)}(r)$ of homogeneous bulk fluids at density ρ_b are obtained from simulated radial distribution functions $g(r)$ through the bulk Ornstein-Zernike equation

$$c_b^{(2)}(r) = \frac{1}{2\pi^2} \int_0^\infty \frac{\sin(kr)}{kr} \left(\frac{\hat{h}(k)}{1 + \rho_b \hat{h}(k)} \right) k^2 dk, \quad (3)$$

with $\hat{h}(k)$ the Fourier transform of the total correlation function $h(r) = g(r) - 1$ [8, 17]. Thus we train our neural network such that its Hessian $\partial^2 F_\theta^{(2)} / \partial \rho_i \partial \rho_j$ represents well the laterally integrated direct correlation function

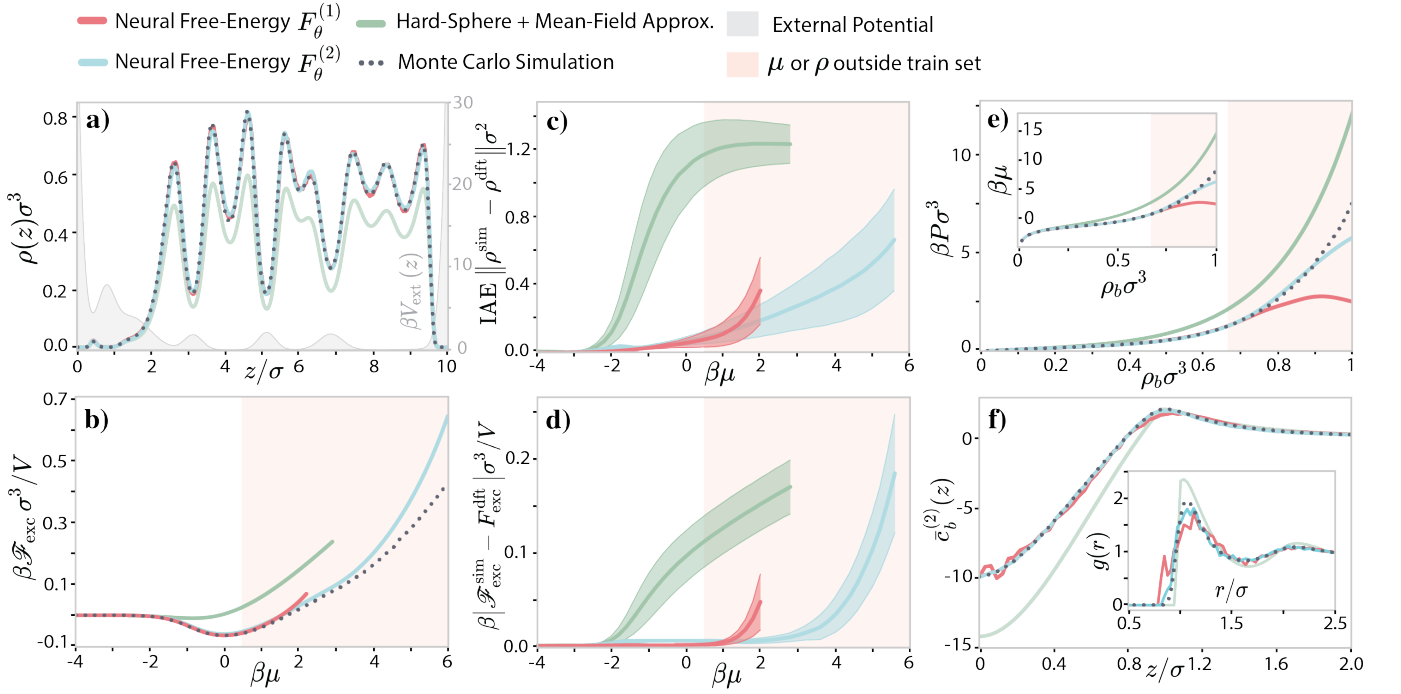


FIG. 2: Evaluation of neural free-energy functionals $F_\theta^{(1)}$ and $F_\theta^{(2)}$, where $F_\theta^{(1)}$ is optimized by matching inhomogeneous one-body densities and $F_\theta^{(2)}$ by pair-correlation matching in the homogeneous bulk. **a)** Density profiles of a Lennard-Jones system in a planar geometry characterized by an external potential (shown in gray) at a chemical potential of $\beta\mu = 0$ obtained from DFT using $F_\theta^{(1)}$ and $F_\theta^{(2)}$ and the mean-field approximation $F_{\text{exc}}^{\text{MF}}$, along with the simulated density profile. **b)** Comparison of the free-energy estimates using $F_\theta^{(1)}$, $F_\theta^{(2)}$, and $F_{\text{exc}}^{\text{MF}}$ for the specific external potential shown in a), for the same chemical potential of $\beta\mu = 0$. **c)** Integrated absolute error (IAE) between density profiles obtained from DFT using $F_\theta^{(1)}$, $F_\theta^{(2)}$, and $F_{\text{exc}}^{\text{MF}}$, along with the densities sampled from simulation. **d)** Absolute error of the excess free energy from DFT and simulations. **c)/d)** Data is shown for 150 distinct external potentials, evaluated across the range $-4 < \beta\mu < 6$, with steps of $\Delta\beta\mu = 0.1$. The area of the mean \pm standard deviation is colored. The error is shown up to the point where the DFT iterations stop to converge to a solution within 1000 iterations. **e)** The pressure and the chemical potential obtained from DFT and simulations. **f)** The laterally integrated direct correlation function $\bar{c}_b^{(2)}(z)$ at $\rho_b\sigma^3 = 0.62$ and the radial distribution function $g(r)$ obtained from simulation and DFT.

obtained from homogeneous bulk simulations [17]. We will refer to this approach as pair-correlation matching.

We illustrate the power of this methodology for systems interacting with a Lennard-Jones potential truncated at $r_{\text{cut}} = 4\sigma$ with σ the particle diameter, shifted upwards by $\epsilon_{\text{cut}} = 0.98 \cdot 10^{-3}\epsilon$ with ϵ the well depth, at a temperature $k_B T/\epsilon = 2$, i.e. above the critical point. Setting $\Lambda = \sigma$ throughout, we perform grand-canonical Monte Carlo (GCMC) simulations of homogeneous bulk systems at a variety of chemical potentials $\beta\mu \in [-4, 0.5]$, resulting in bulk densities $\rho_b\sigma^3 \in [0.02, 0.67]$. We employ 10^9 trial moves in a cubic box with an edge length $L = 10\sigma$ (hence with area $A = L^2$ and volume $V = L^3$) and apply periodic boundary conditions. We sample $g(r)$ and ρ_b and convert each $g(r)$ to $\bar{c}_b^{(2)}(z)$ using Eqs. (2) and (3) with a grid-spacing $\Delta z = \sigma/32$. We create a data set of 800 combinations of $\bar{c}_b^{(2)}(z)$ and ρ_b , from which we learn the parameters θ of $F_\theta^{(2)}$. The neural network architecture of $F_\theta^{(2)}$ is a six-layer convolutional neural network with periodic padding [18] to match the sys-

tem's periodic boundary conditions. Each convolution uses a kernel size of 3 with a dilation rate of 3. The number of channels per hidden layer is configured as follows: [16, 16, 32, 32, 64, 64], such that θ consists of 24.4K parameters [17].

To evaluate the accuracy of our neural excess free-energy functional $F_\theta^{(2)}$, we compare it to the Van der Waals-like mean-field approximation $F_{\text{exc}}^{\text{MF}}$, which treats the attractions of Lennard-Jones particles as a perturbation on the hard-sphere system, as implemented in PyDFTlj [1]. We use the White-Bear mark II version of FMT for the excess free energy of the hard-sphere system [19]. Additionally, we compare to $F_\theta^{(1)}$, which is a neural functional trained by minimization of the error between $(1/\Delta z)\partial F_\theta^{(1)}/\partial\rho_i$ and $\delta\mathcal{F}_{\text{exc}}/\delta\rho(z_i)$ rather than by pair-correlation matching. This neural functional is trained on a dataset of 800 non-uniform densities, subjected to the same set of chemical potentials as before [17]. By approximating $\delta\mathcal{F}_{\text{exc}}/\delta\rho(z_i)$ by the gradient $(1/\Delta z)\partial F_\theta^{(n)}/\partial\rho_i$ for $n = 1$ and 2, both neural func-

tionals are applied in Picard iterations [20–22] to obtain DFT estimates for the equilibrium density profiles of inhomogeneous systems according to Eq. (1).

The DFT results for an exemplary external potential at $\beta\mu = 0$ are shown in Fig. 2a, where we observe that the neural functionals $F_\theta^{(1)}$ and $F_\theta^{(2)}$ provide similar estimates, both outperforming $F_{\text{exc}}^{\text{MF}}$. For the same external potential, we evaluate the accuracy of DFT estimates for the free energy for a range of chemical potentials $-4 < \beta\mu < 6$ (Fig. 2b). We compare with the excess free energy obtained from GCMC simulations through thermodynamic integration [17]. We observe that both neural functionals outperform $F_{\text{exc}}^{\text{MF}}$ within the range of μ values in the training set, exhibiting good agreement with the simulations. The DFT estimates are shown until the DFT iterations diverge and errors become unmanageable. This reveals that $F_\theta^{(1)}$ diverges rapidly when extrapolating beyond the training set, even earlier than $F_{\text{MF}}^{\text{exc}}$. In contrast, $F_\theta^{(2)}$ is capable of converging to a solution far beyond the trained μ range.

For a more detailed comparison of the performance of the free-energy functionals for various inhomogeneous systems, we performed separate DFT calculations for 150 distinct external potentials, evaluated across the range $-4 < \beta\mu < 6$. For both the density estimates (Fig. 2c) and the free-energy estimates (Fig. 2d), we observe excellent agreement between the $F_\theta^{(1)}$ and $F_\theta^{(2)}$ functionals and simulated data. They demonstrate similar performance for μ values within the training set range, and outperform the $F_{\text{exc}}^{\text{MF}}$ functional for all evaluated external potentials (Fig. 2). Again, we observe that $F_\theta^{(2)}$ surpasses $F_\theta^{(1)}$ when extrapolating beyond the μ range encountered during training.

Additionally, the free-energy functionals can be applied in a uniform density setting to obtain access to the bulk pressure

$$P(\rho_b) = \left(\frac{\delta \mathcal{F}_{\text{exc}}}{\delta \rho} \Big|_{\rho_b} + k_B T \right) \rho_b - \mathcal{F}_{\text{exc}}[\rho_b]/V, \quad (4)$$

and the chemical potential μ following Eq. (1). Again, we find excellent agreement of both neural functionals with simulations within the training set, and superior agreement of $F_\theta^{(2)}$ at higher densities, as shown in Fig. 2e. Lastly, we demonstrate that $F_\theta^{(2)}$ compared to both $F_\theta^{(1)}$ and $F_{\text{MF}}^{\text{exc}}$ provides accurate estimates for the laterally integrated direct correlation function $\bar{c}_b^{(2)}(z)$ and the radial distribution function $g(r)$ as shown in Fig. 2f for $\rho_b \sigma^3 = 0.62$. Here, we approximate $\bar{c}_b^{(2)}(z)$ by $(-\beta/A(\Delta z)^2) \partial^2 F_\theta / \partial \rho_i \partial \rho_j$ with $z = |z_i - z_j|$. To derive the radial distribution function, we first numerically calculate $c_b^{(2)}(r)$ from $\bar{c}_b^{(2)}(z)$ using

$$-\frac{1}{2\pi} \left(\frac{1}{z} \frac{d\bar{c}_b^{(2)}(z)}{dz} \right) \Big|_{z=r} = c_b^{(2)}(r). \quad (5)$$

We then obtain $g(r)$ using the Ornstein-Zernike equation. To suppress artefacts stemming from numerical transformations in the region for $g(r) \rightarrow 0$, we apply a noise-reducing filter [17].

Summarizing, our results lead to the remarkable observation that our neural free-energy functional $F_\theta^{(2)}$ is robust and accurate for non-uniform density systems, even far beyond its training range, solely by training on pair correlation functions in homogeneous bulk systems. These observations show that generating a large dataset of density profiles across a wide range of external potentials is not necessary to train an accurate neural free-energy functional. Instead, only a dataset of radial distribution functions from bulk systems is needed. This work thus represents a significant advancement in the field of cDFT, enabling applications to systems in arbitrary three-dimensional geometries, as accurate sampling of three-dimensional density profiles is considerably more expensive than sampling the one-dimensional radial distribution function. We expect that extensions of this method to mixtures of simple fluids and to particles with orientation degrees of freedom [14] should be possible.

Unlike the density profile, the radial distribution function is experimentally available through X-ray diffraction. This suggests the potential to use pair-correlation matching to directly construct the excess free energy of a molecular system from the true radial distribution function obtained from experiments, bypassing the dependence on simulations with model interaction approximations such as the Lennard-Jones potential.

In conclusion, this work introduces a generic machine learning approach to obtain classical free-energy functionals through pair-correlation matching. We showed how to learn a neural-network representation of the excess free-energy functional of a generic simple fluid by solely learning the direct correlations from the radial distribution function obtained from uniform density simulations. Through pair-correlation matching, we attain a neural free-energy functional that enables simultaneous and direct access to both the excess free energy and the density of a system of interacting particles in any external environment.

ACKNOWLEDGEMENTS

The authors acknowledge the University of Amsterdam Data Science Centre for financial support. M.D. acknowledges funding from the European Research Council (ERC) under the European Union’s Horizon 2020 Research and Innovation Program (Grant Agreement No. ERC-2019-ADG 884902 SoftML). J.W.M. acknowledges funding from the European Union’s Horizon Framework Programme (Grant agreement ID: 101120237).

-
- [1] E. d. A. Soares, A. G. Barreto Jr., and F. W. Tavares, Classical Density Functional Theory Reveals Structural Information of H₂ and CH₄ Fluids Adsorbed in MOF-5 (2023), arxiv:2303.11384 [cond-mat, physics:physics].
- [2] F. Guo, Y. Liu, J. Hu, H. Liu, and Y. Hu, Classical density functional theory for gas separation in nanoporous materials and its application to CH₄/H₂ separation, *Chem. Eng. Sci.* **149**, 14 (2016).
- [3] F. Guo, Y. Liu, J. Hu, H. Liu, and Y. Hu, Fast screening of porous materials for noble gas adsorption and separation: A classical density functional approach, *Phys. Chem. Chem. Phys.* **20**, 28193 (2018).
- [4] F. Guo, Y. Liu, J. Hu, H. Liu, and Y. Hu, Screening of Porous Materials for Toxic Gas Adsorption: Classical Density Functional Approach, *Ind. Eng. Chem. Res.* **59**, 14364 (2020).
- [5] J. Fu, Y. Tian, and J. Wu, Classical density functional theory for methane adsorption in metal-organic framework materials, *AIChE J.* **61**, 3012 (2015).
- [6] Y. Liu and H. Liu, Classical Density Functional Theory for Fluids Adsorption in MOFs, in *Metal-Organic Frameworks*, edited by F. Zafar and E. Sharmin (InTech, 2016).
- [7] R. Evans, The nature of the liquid-vapour interface and other topics in the statistical mechanics of non-uniform, classical fluids, *Adv. Phys.* **28**, 143 (1979).
- [8] J.-P. Hansen and I. R. McDonald, Theory of Simple Liquids, in *Theory of Simple Liquids* (Elsevier, 2013).
- [9] R. Roth, Fundamental measure theory for hard-sphere mixtures: A review, *J. Phys. Condens. Matter* **22**, 10.1088/0953-8984/22/6/063102 (2010).
- [10] P. Cats, R. Evans, A. Härtel, and R. Van Roij, Primitive model electrolytes in the near and far field: Decay lengths from DFT and simulations, *J. Chem. Phys.* **154**, 10.1063/5.0039619 (2021), arxiv:2012.02713.
- [11] S. C. Lin and M. Oettel, A classical density functional from machine learning and a convolutional neural network, *SciPost Phys.* **6**, 1 (2019), arxiv:1811.05728.
- [12] P. Cats, S. Kuipers, S. De Wind, R. Van Damme, G. M. Coli, M. Dijkstra, and R. Van Roij, Machine-learning free-energy functionals using density profiles from simulations, *APL Mater.* **9**, 10.1063/5.0042558 (2021), arxiv:2101.01942.
- [13] F. Sammüller, S. Hermann, D. De Las Heras, and M. Schmidt, Neural functional theory for inhomogeneous fluids: Fundamentals and applications, *Proc. Natl. Acad. Sci. USA* **120**, e2312484120 (2023).
- [14] A. Simon, J. Weimar, G. Martius, and M. Oettel, Machine Learning of a Density Functional for Anisotropic Patchy Particles, *J. Chem. Theory Comput.* **20**, 1062 (2024).
- [15] A. G. Baydin, B. A. Pearlmutter, A. A. Radul, and J. M. Siskind, Automatic differentiation in machine learning: a survey, *J. Machine Learn. Res.* **18**, 1 (2018).
- [16] A. Paszke, S. Gross, S. Chintala, G. Chanan, E. Yang, Z. DeVito, Z. Lin, A. Desmaison, L. Antiga, and A. Lerer, Automatic differentiation in PyTorch, NIPS Autodiff Workshop (2017).
- [17] J. Dijkman, M. Dijkstra, R. van Roij, M. Welling, J.-W. van de Meent, and B. Ensing, Supplementary Material of Learning Neural Free-Energy Functionals with Pair-Correlation Matching, (2024), arxiv:2403.15007 [cond-mat].
- [18] A. Alguacil, W. G. Pinto, M. Bauerheim, M. C. Jacob, and S. Moreau, Effects of boundary conditions in fully convolutional networks for learning spatio-temporal dynamics (2021), arxiv:2106.11160 [physics].
- [19] H. Hansen-Goos and R. Roth, Density functional theory for hard-sphere mixtures: The White Bear version mark II, *J. Phys. Condens. Matter* **18**, 8413 (2006).
- [20] R. Roth, Introduction to Density Functional Theory of Classical Systems: Theory and Applications, Lecture Notes (2006).
- [21] M. Edelmann and R. Roth, A numerical efficient way to minimize classical density functional theory, *J. Chem. Phys.* **144**, 074105 (2016).
- [22] J. Mairhofer and J. Gross, Numerical aspects of classical density functional theory for one-dimensional vapor-liquid interfaces, *Fluid Phase Equilibria* **444**, 1 (2017).

Supplementary Material: Learning Neural Free-Energy Functionals with Pair-Correlation Matching

Jacobus Dijkman,^{1,2} Marjolein Dijkstra,³ René van Roij,⁴
Max Welling,² Jan-Willem van de Meent,² and Bernd Ensing^{1,5}

¹*Van 't Hoff Institute for Molecular Sciences, University of Amsterdam, The Netherlands*

²*Informatics Institute, University of Amsterdam, The Netherlands*

³*Debye Institute for Nanomaterials Science, Utrecht University, The Netherlands*

⁴*Institute for Theoretical Physics, Utrecht University, The Netherlands*

⁵*AI4Science Laboratory, University of Amsterdam, The Netherlands*

(Dated: May 15, 2024)

CONTENTS

1. Classical density functional theory	1
2. Pair-correlation matching	1
3. Training on the single-body direct correlation function	3
4. Extended results	4
5. Construction of external potentials	5
6. Obtaining the excess free energy from simulation	6
7. Numerical errors in the radial distribution function	6
8. Sampling in planar geometry systems vs. arbitrary 3D systems	6
References	7

1. CLASSICAL DENSITY FUNCTIONAL THEORY

Classical density functional theory (cDFT) is a grand-canonical framework that relies on the fact that the variational grand potential $\Omega[\rho]$ is uniquely determined by the particle density $\rho(\mathbf{r})$ via

$$\Omega[\rho] = \mathcal{F}[\rho] + \int d\mathbf{r} \rho(\mathbf{r}) (V_{\text{ext}}(\mathbf{r}) - \mu), \quad (\text{S.1})$$

with $\mathcal{F}[\rho]$ representing the intrinsic Helmholtz free-energy functional, $V_{\text{ext}}(\mathbf{r})$ the external potential, and μ the chemical potential. For a given particle-particle interaction and temperature, the unique density functional $\mathcal{F}[\rho]$ determines the thermodynamic and structural equilibrium properties of a system for any chemical potential and external potential. Within cDFT, it is conventional to split the intrinsic free-energy functional into an ideal and excess contribution, $\mathcal{F}[\rho] = \mathcal{F}_{\text{id}}[\rho] + \mathcal{F}_{\text{exc}}[\rho]$. The ideal-gas contribution is exactly known as

$$\mathcal{F}_{\text{id}}[\rho] = \frac{1}{\beta} \int d\mathbf{r} \rho(\mathbf{r}) (\ln \rho(\mathbf{r}) \Lambda^3 - 1), \quad (\text{S.2})$$

with $\beta = 1/k_B T$ and Λ the thermal wavelength.

Mathematical proofs exist [1] stating that (i) the equilibrium density profile, denoted here as $\rho_0(\mathbf{r})$, minimizes $\Omega[\rho]$, and (ii) the equilibrium grand potential equals $\Omega[\rho_0]$. Clearly, once $\mathcal{F}[\rho]$ for the system of interest is known, the Euler-Lagrange equation $\delta\Omega[\rho]/\delta\rho(\mathbf{r})|_{\rho_0} = 0$ can be solved to find $\rho_0(\mathbf{r})$ and $\Omega[\rho_0]$. The Euler-Lagrange equation takes the form

$$\rho_0(\mathbf{r}) = \frac{1}{\Lambda^3} \exp \left(\beta\mu - \beta \left. \frac{\delta\mathcal{F}_{\text{exc}}[\rho]}{\delta\rho(\mathbf{r})} \right|_{\rho=\rho_0} - \beta V_{\text{ext}}(\mathbf{r}) \right). \quad (\text{S.3})$$

This self-consistency relation can be leveraged to find $\rho_0(\mathbf{r})$ through recursive iteration.

2. PAIR-CORRELATION MATCHING

We train a convolutional neural network to directly approximate the excess free energy $\mathcal{F}_{\text{exc}}[\rho]$, enabling the straightforward calculation of functional derivatives by (auto-)differentiating the neural functional with respect to its inputs. Rather than approximating the free energy directly, we train the neural functional by optimizing an objective that matches the Hessian of the network to a

direct correlation function that is computed from short simulations of homogeneous bulk systems. We refer to this approach as pair-correlation matching. In this work, we focus on 3D systems in a planar geometry, where the excess free energy of a system of area A is a functional of the density $\rho(z)$, which is constant across any plane parallel to the xy -plane, i.e. $\rho(z) = \rho(x, y, z)$ with $\rho(x, y, z) = \rho(x', y', z)$ for all $(x, y), (x', y')$ within the confines of A . We represent the excess free-energy functional $\mathcal{F}_{\text{exc}}[\rho]$ as a neural network $F_{\theta}^{(2)}(\rho_1, \dots, \rho_n)$, with ρ_i the density at grid point z_i for $i \in \{1, \dots, n\}$, network parameters θ , and where the upper index ‘(2)’ indicates that the neural network is optimized for pair correlations of bulk systems as obtained from simulations.

The functional derivative $\delta\mathcal{F}_{\text{exc}}/\delta\rho$ evaluated at z_i is defined as the limit of the partial derivative $\lim_{\Delta z \rightarrow 0} (1/\Delta z) \partial\mathcal{F}_{\text{exc}}/\partial\rho_i$ with $\rho_i = \rho(z_i)$ and Δz the (uniform) grid spacing. We leverage this relationship by employing automatic differentiation (autodiff) to approximate the first and second functional derivatives of $\mathcal{F}_{\text{exc}}[\rho]$ on a finite grid by $(1/\Delta z) \partial F_{\theta}^{(2)}/\partial\rho_i$ and $(1/\Delta z)^2 \partial^2 F_{\theta}^{(2)}/\partial\rho_i \partial\rho_j$, respectively. We target the approximation of the second functional derivative in homogeneous bulk systems with bulk densities ρ_b as our primary optimization objective, i.e. we minimize the difference between $(1/\Delta z)^2 \partial^2 F_{\theta}^{(2)}/\partial\rho_i \partial\rho_j|_{\rho_b}$ and $\delta^2\mathcal{F}_{\text{exc}}/\delta\rho(z_i)\delta\rho(z_j)|_{\rho_b}$.

To train our neural functional according to this optimization objective, we require ground-truth examples of $\delta^2\mathcal{F}_{\text{exc}}/\delta\rho(z_i)\delta\rho(z_j)|_{\rho_b}$. We obtain these examples by sampling the radial distribution function $g(r)$ from simulations of homogeneous bulk systems and applying the Ornstein-Zernike equation to obtain $\delta^2\mathcal{F}_{\text{exc}}/\delta\rho(z_i)\delta\rho(z_j)|_{\rho_b}$ from $g(r)$. Key to this transformation is the two-body direct correlation function, which is defined in terms of the second functional derivative as

$$c^{(2)}(\mathbf{r}, \mathbf{r}') = -\beta \frac{\delta^2\mathcal{F}_{\text{exc}}[\rho]}{\delta\rho(\mathbf{r})\delta\rho(\mathbf{r}')}, \quad (\text{S.4})$$

for systems with arbitrary geometry. In a uniform and isotropic bulk fluid, $c^{(2)}(\mathbf{r}, \mathbf{r}') = c_b^{(2)}(r)$ only depends on the distance between two points,

$$r = |\mathbf{r} - \mathbf{r}'| = \sqrt{(x - x')^2 + (y - y')^2 + (z - z')^2}. \quad (\text{S.5})$$

In such a system, we obtain the direct correlation function $c_b^{(2)}(r)$ from the radial distribution function $g(r)$ by first calculating the total correlation function $h(r) = g(r) - 1$ and then applying the bulk Ornstein-Zernike equation

$$c_b^{(2)}(r) = \frac{1}{2\pi^2} \int_0^\infty \frac{\sin(kr)}{kr} \left(\frac{\hat{h}(k)}{1 + \rho\hat{h}(k)} \right) k^2 dk, \quad (\text{S.6})$$

with $\hat{h}(k)$ the Fourier transform of the total correlation function $h(r)$. Since we consider systems in planar geometry, we integrate Eq. (S.4) with respect to

the x and y coordinates and define polar coordinates $R = \sqrt{(x - x')^2 + (y - y')^2}$ to obtain an expression for the laterally integrated direct correlation function $\bar{c}_b^{(2)}(z)$ in terms of $c_b^{(2)}(r)$, i.e.,

$$\begin{aligned} \bar{c}^{(2)}(|z - z'|) &= \frac{1}{A} \int dx dy \int dx' dy' c_b^{(2)}(|\mathbf{r} - \mathbf{r}'|) \\ &= \int_0^\infty dR 2\pi R c_b^{(2)}(\sqrt{R^2 + (z - z')^2}) \\ &= \int_{|z - z'|}^\infty dr 2\pi r c_b^{(2)}(r) \\ &= \frac{-\beta}{A} \frac{\delta^2\mathcal{F}_{\text{exc}}[\rho]}{\delta\rho(z)\delta\rho(z')} \end{aligned} \quad (\text{S.7})$$

Here we assume that $c^{(2)}(r)$ trends towards zero for r significantly smaller than R_{max} , with $R_{\text{max}} = L/2$ for a cubic box of edge length L . Our findings indicate that for systems with an edge length of $L = 10\sigma$ and bulk density $\rho_b\sigma^3$ approximately greater than 0.67, the value of $c^{(2)}(R_{\text{max}})$ is too significant for this assumption to hold and for the numerically obtained transformation to remain valid. Consequently, we restrict our training data to systems where $\rho_b\sigma^3$ is less than or equal to 0.67.

With Eq. (S.7), we have arrived at an expression that enables us to construct a training set, by computing $\delta^2\mathcal{F}_{\text{exc}}/\delta\rho(z_i)\delta\rho(z_j)|_{\rho_b}$ from sampled $g(r)$ through $c_b^{(2)}(r)$:

$$\frac{-\beta}{A} \frac{\delta^2\mathcal{F}_{\text{exc}}[\rho]}{\delta\rho(z_i)\delta\rho(z_j)} = \int_{|z_i - z_j|}^\infty dr 2\pi r c_b^{(2)}(r), \quad (\text{S.8})$$

We now construct an optimization objective that minimizes the distance between $(1/\Delta z)^2 \partial^2 F_{\theta}^{(2)}/\partial\rho_i \partial\rho_j$ and $\delta^2\mathcal{F}_{\text{exc}}/\delta\rho(z_i)\delta\rho(z_j)$, i.e.,

$$L(\theta) = \sum_{i,j} \left(\int_{|z_i - z_j|}^\infty dr 2\pi r c_b^{(2)}(r) + \frac{\beta}{A(\Delta z)^2} \frac{\partial^2 F_{\theta}^{(2)}}{\partial\rho_i \partial\rho_j} \right)^2 \quad (\text{S.9})$$

Optimizing for $\delta^2\mathcal{F}_{\text{exc}}/\delta\rho(z_i)\delta\rho(z_j)$ means we lack information on the integration constant $\delta\mathcal{F}_{\text{exc}}/\delta\rho_0 = C$, akin to missing the integration constant C when integrating df/dx to find $f(x)$, e.g.,

$$f(x) = \int dx \frac{df}{dx} + C. \quad (\text{S.10})$$

Therefore, we also apply an additional regularization loss term during training that minimizes the difference between the uniform $\delta\mathcal{F}_{\text{exc}}/\delta\rho(z_i)|_{\rho_b}$ corresponding to bulk densities ρ_b and $\partial F_{\theta}^{(2)}/\partial\rho_i|_{\rho_b}$, given as

$$L_{\text{reg}}(\theta) = \frac{1}{n} \sum_i \left(\frac{1}{\Delta z} \cdot \frac{\partial F_{\theta}^{(2)}}{\partial\rho_i} - \frac{\delta\mathcal{F}_{\text{exc}}}{\delta\rho(z_i)} \Big|_{\rho_b} \right)^2, \quad (\text{S.11})$$

where n denotes the number of grid points and $\delta\mathcal{F}_{\text{exc}}/\delta\rho(z_i)$ is obtained from sampled bulk densities according to Eq. (S.13), as discussed in section 3 of the Supplementary Material.

It is important to mention that we similarly cannot obtain the integration constant $\mathcal{F}_{\text{exc}}[0] = C$ from $\delta\mathcal{F}_{\text{exc}}/\delta\rho(z_i)$ in the case we seek access to $\mathcal{F}_{\text{exc}}[\rho]$ after training. However, since we know the low-density limit $\mathcal{F}_{\text{exc}}[0] = 0$, we can correct the output of our neural network functional such that $F_{\theta}^{(2)}[\rho] - C$ approximates $\mathcal{F}_{\text{exc}}[\rho]$, with $C = F_{\theta}^{(2)}[0]$.

The training procedure of pair-correlation matching is summarized in Algorithm 1. Here, we represent $c_b^{(2)}(z_i)$ numerically as $c_{b,i}^{(2)}$ with $c_{b,i}^{(2)} = c_{b,n-i}^{(2)}$ due to periodic boundary conditions. Similarly, we represent the sampled bulk density $\rho_b(z_i)$ numerically as $\rho_{b,i}$, where $\rho_{b,i} = \rho_{b,j}$, $\forall i, j \in n$.

For the implementation of pair-correlation matching in this work, we construct a dataset from simulations of 10^9 trial moves in a cubic box with an edge length of 10σ subject to periodic boundary conditions and a $\sigma/32$ grid-spacing. All simulations are carried out at distinct chemical potentials $\beta\mu \in [-4, 0.5]$, resulting in a maximum bulk density of $\rho_b\sigma^3 = 0.67$ and a minimum bulk density of $\rho_b\sigma^3 = 0.02$ within the training set.

We employ a convolutional neural network with periodic and dilated convolutions, each with a kernel size of 3, a dilation of 2, and 6 layers. The number of channels per layer is set as $N_{\text{channels}} = [16, 16, 32, 32, 64, 64]$. This network takes as input an array of $n = 320$ values of $\{\rho_i\}_{i=0}^n$ per datapoint and produces a single scalar output, $F_{\theta}^{(2)}$. The model is trained for 180 epochs, taking approximately ~ 30 minutes on an Nvidia RTX 4070 GPU. To reduce computational cost during training, we compute a randomly sampled subset of $m = 10$ rows of the Hessian $\{\{\partial^2 F_{\theta}^{(2)}/\partial\rho_i\partial\rho_j\}_{i=0}^n\}_{j=0}^m$ per loss evaluation.

3. TRAINING ON THE SINGLE-BODY DIRECT CORRELATION FUNCTION

Instead of using pair-correlation matching, we can train a neural free-energy functional $F_{\theta}^{(1)}$ by minimizing the error between $\delta\mathcal{F}_{\text{exc}}/\delta\rho(z_i)$ and $(1/\Delta z)\partial F_{\theta}^{(1)}/\partial\rho_i$, as illustrated in Fig. S.1. We denote this neural functional as $F_{\theta}^{(1)}$, as the first functional derivative of the excess free energy is associated with the one-body direct correlation function by $c^{(1)}(x, y, z) = -\beta\delta\mathcal{F}_{\text{exc}}/\delta\rho(x, y, z)$.

We can obtain the first functional derivative of the excess free energy from the equilibrium density by rearranging Eq. (S.3):

$$-\beta\frac{\delta\mathcal{F}_{\text{exc}}}{\delta\rho(x, y, z)} = \ln\Lambda^3\rho(x, y, z) + \beta V_{\text{ext}}(x, y, z) - \beta\mu. \quad (\text{S.12})$$

Algorithm 1: Pair-Correlation Matching

Data: $\mathcal{D} = \{\{c_{b,i}^{(2),0}, \rho_{b,i}^0\}_{i=0}^n, \dots, \{c_{b,i}^{(2),N}, \rho_{b,i}^N\}_{i=0}^n\}$ containing N pair-correlation functions $\{c_{b,i}^{(2)}\}_{i=0}^n$; N bulk density profiles $\{\rho_{b,i}\}_{i=0}^n$; regularization factor $\alpha = 0.01$.

Result: trained neural functional $F_{\theta}^{(2)}(\{\rho_i\}_{i=0}^n)$.

for epoch **do**

for each $\{c_{b,i}^{(2)}, \rho_{b,i}\}_{i=0}^n$ in \mathcal{D} **do**

compute neural network output $F_{\theta}^{(2)}(\{\rho_{b,i}\}_{i=0}^n)$;

compute $\{\partial F_{\theta}^{(2)}/\partial\rho_i\}_{i=0}^n$ with autodiff;

sample batch $\mathcal{B} = \{\partial F_{\theta}^{(2)}/\partial\rho_i\}_{i=0}^m$ with $m \in n$;

for $\partial F_{\theta}^{(2)}/\partial\rho_i$ in \mathcal{B} **do**

compute $\{\partial^2 F_{\theta}^{(2)}/\partial\rho_i\partial\rho_j\}_{j=0}^n$ with autodiff;

compute $\{\delta^2\mathcal{F}_{\text{exc}}/\delta\rho(z_i)\delta\rho(z_j)\}_{j=0}^n$ from $\{c_{b,i}^{(2)}\}_{i=0}^n$ with Eq. (S.8);

end

$L(\theta) = \frac{1}{nm} \sum_{i,j} (\delta^2\mathcal{F}_{\text{exc}}/\delta\rho(z_i)\delta\rho(z_j) - (1/\Delta z)^2 \partial^2 F_{\theta}^{(2)}/\partial\rho_i\partial\rho_j)^2$;

compute $\{\delta^2\mathcal{F}_{\text{exc}}/\delta\rho(z_i)\}_{i=0}^n$ with Eq. (S.13);

$L_{\text{reg}}(\theta) = \frac{1}{n} \sum_i \left(\delta\mathcal{F}_{\text{exc}}/\delta\rho(z_i) - (1/\Delta z)\partial F_{\theta}^{(2)}/\partial\rho_i \right)^2$;

$L(\theta) = L(\theta) + \alpha \cdot L_{\text{reg}}(\theta)$;

update parameters $\theta \leftarrow \text{Optimizer}(\theta, \nabla_{\theta} L(\theta))$;

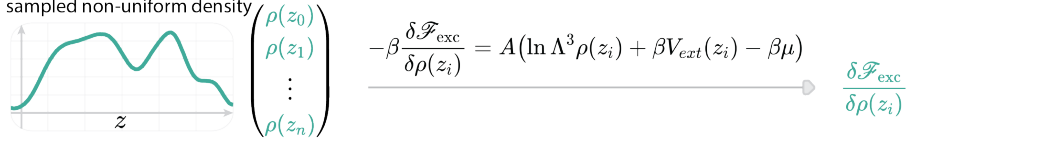
end

We consider 3D systems in a planar geometry, where the excess free energy of a system with area A is a functional of the density $\rho(z)$, which is constant across any plane parallel to the xy -plane, i.e., $\rho(z) = \rho(x, y, z)$ with $\rho(x, y, z) = \rho(x', y', z)$ for all $(x, y), (x', y')$ within the confines of A . For such a system, we can write

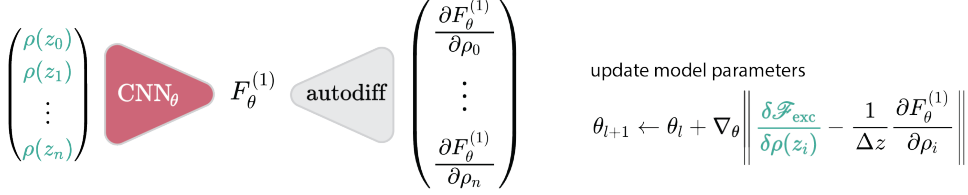
$$-\beta\frac{\delta\mathcal{F}_{\text{exc}}}{\delta\rho(z)} = A(\ln\Lambda^3\rho(z) + \beta V_{\text{ext}}(z) - \beta\mu). \quad (\text{S.13})$$

This means that we can obtain $\delta\mathcal{F}_{\text{exc}}/\delta\rho(z)$ by sampling equilibrium densities from simulation. We sample density profiles of inhomogeneous systems of Lennard-Jones particles above the critical point at a temperature $k_B T/\epsilon = 2$. We construct a dataset from simulations of 10^9 trial moves in a cubic box with an edge length of 10σ subject to periodic boundary conditions and a $\sigma/32$ grid-spacing. All simulations are conducted at distinct chemical potentials $\beta\mu \in [-4, 0.5]$ and a maximum local density of $\rho(z)\sigma^3 = 0.67$. The choice of external potentials is explained in section 5 of the Supplementary Material. We use the same convolutional neural network architecture as for the neural functional $F_{\theta}^{(2)}$. The model is trained for 5000 epochs, requiring approximately 100 minutes on an Nvidia RTX 4070 GPU. The training procedure is summarized in Algorithm 2.

1. Generate training data from MC simulations



2. Train the neural network



3. Classical DFT at fixed $\beta\mu$ and $\beta V^{\text{ext}}(z)$

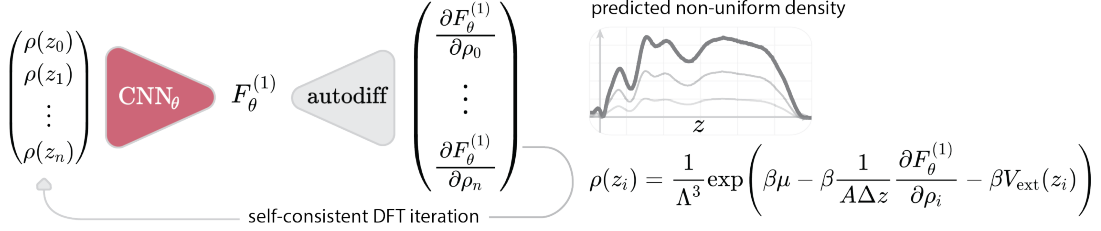


FIG. S.1: The neural free-energy functional $F_\theta^{(1)}$ is trained by fitting the gradient of the model output with respect to the input to the first functional derivative of the excess free energy as obtained from simulation, after which it can be applied within the classical Density Functional Theory (cDFT) framework. **1.** Non-uniform densities are sampled from Monte Carlo simulations of Lennard-Jones particles subjected to inhomogeneous external potentials, from which $\delta\mathcal{F}_{\text{exc}}/\delta\rho(z_i)$ is derived. **2.** Through automatic differentiation (autodiff), the neural functional is optimized to fit the gradient of the model output with respect to input density profiles to $\delta\mathcal{F}_{\text{exc}}/\delta\rho(z_i)$. **3.** The optimized model can then be applied in cDFT to obtain the non-uniform equilibrium densities and the excess free energy for a system of Lennard-Jones particles subjected to inhomogeneous external potentials.

Algorithm 2: Training on $\delta\mathcal{F}_{\text{exc}}/\delta\rho(z)$

Data: train dataset $\mathcal{D} = \{\{\rho_i^0\}_{i=0}^n, \dots, \{\rho_i^N\}_{i=0}^n\}$ consisting of N density profiles $\{\rho_i\}_{i=0}^n$ evaluated at gridpoints $\{z_i\}_{i=0}^n$.

Result: trained neural network model $F_\theta^{\text{exc}}(\{\rho_i\}_{i=0}^n)$.

for dataset iterations **do**

for each $\rho = \{\rho_i\}_{i=0}^n$ in \mathcal{D} **do**

 generate model output scalar $F_\theta^{(1)}(\{\rho_i\}_{i=0}^n)$;

 compute $\{\partial F_\theta^{(1)}/\partial\rho_i\}_{i=0}^n$ with autodiff;

 compute $\{\delta\mathcal{F}_{\text{exc}}/\delta\rho(z_i)\}_{i=0}^n$ with Eq. (S.13);

$L_\theta = \frac{1}{n} \sum_{i=0}^n (\delta\mathcal{F}_{\text{exc}}/\delta\rho(z_i) - (1/\Delta z) \partial F_\theta^{(1)}/\partial\rho_i)^2$;

 update parameters $\theta \leftarrow \text{Optimizer}(\theta, \nabla_\theta L_\theta)$;

end

end

4. EXTENDED RESULTS

In addition to Figure 2a in the main text, we present additional examples of DFT predictions for various external potentials, as shown in Fig. S.2. In this figure, the columns depict increasing chemical potentials from left

to right: $\beta\mu = -3$ for Fig. S.2a and S.2d; $\beta\mu = 0$ for Fig. S.2b and S.2e; and $\beta\mu = 3$ for Fig. S.2c and S.2f.

The external potentials shown in Fig. S.2a–c are generated using a set of Gaussian potentials (Fig. S.2a and S.2c), and a combination of Gaussian potentials and a well-potential (Fig. S.2b), as described in the section 5 of the Supplementary Material. We observe that both neural functionals $F_\theta^{(1)}$ and $F_\theta^{(2)}$ provide accurate predictions for $\beta\mu = -3$ and $\beta\mu = 0$, both outperforming $F_{\text{exc}}^{\text{MF}}$. However, $F_{\text{exc}}^{\text{MF}}$ and $F_\theta^{(1)}$ both fail to converge to a solution for $\beta\mu = 3$ (Fig. S.2f), which lies far outside the training set range of $\beta\mu \in [-4, 0.5]$. While $F_\theta^{(2)}$ is also trained with (uniform) densities up to $\beta\mu = 0.5$, it is still capable of producing relatively accurate predictions for $\beta\mu = 3$.

Additionally, we test the performance of the neural functionals on a number of atypical external potentials that are in no way related to the family of external potentials used elsewhere in this work (Fig. S.2d–f). Here we observe that both neural functionals $F_\theta^{(1)}$ and $F_\theta^{(2)}$ still perform well for these potentials for $\beta\mu = -3$ and $\beta\mu = 0$. Again, $F_{\text{exc}}^{\text{MF}}$ and $F_\theta^{(1)}$ fail to converge to a

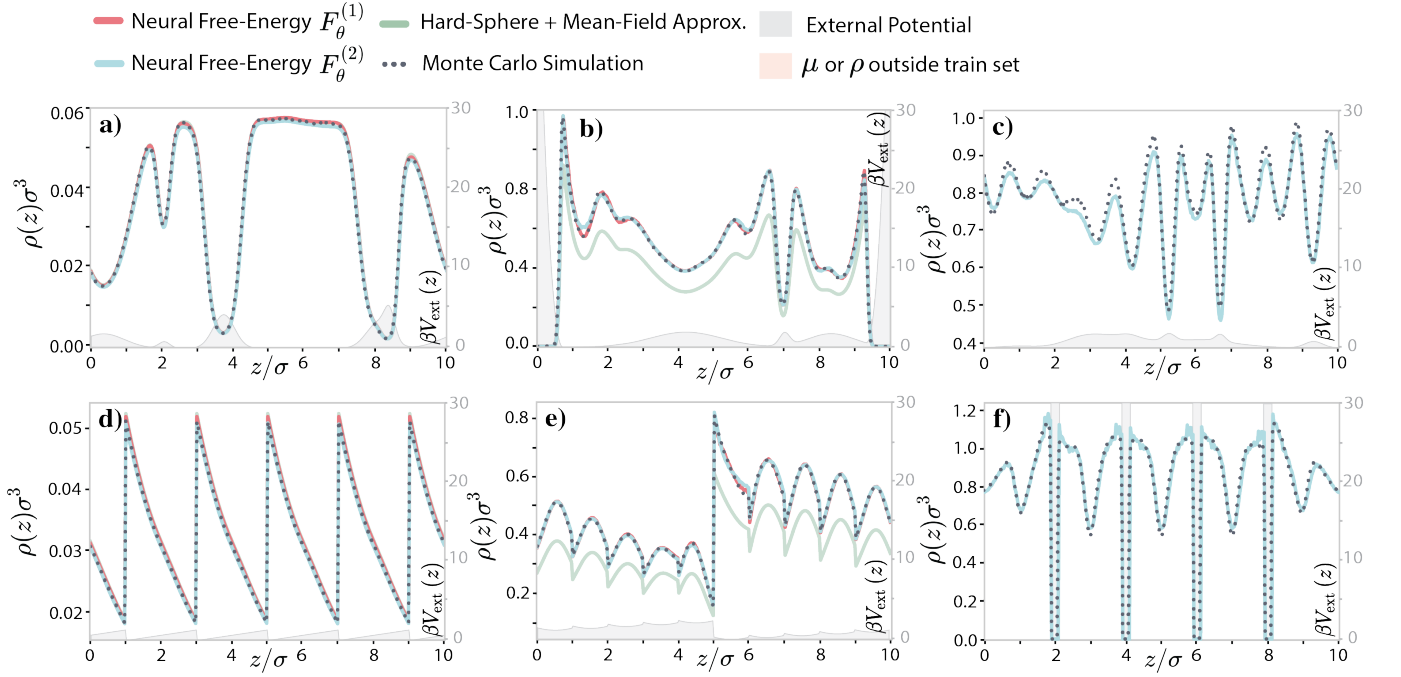


FIG. S.2: Evaluation of the neural free-energy functionals $F_\theta^{(1)}$ and $F_\theta^{(2)}$. $F_\theta^{(1)}$ is optimized based on one-body correlation functions, while $F_\theta^{(2)}$ is optimized using pair-correlation matching. Comparison of the estimates for an inhomogeneous density profile through classical DFT between the functionals $F_\theta^{(1)}$, $F_\theta^{(2)}$ and $F_{\text{exc}}^{\text{MF}}$, which represents the analytical approximation of the White-Bear mark II version of Fundamental Measure Theory (FMT) combined with a mean-field approximation for the attractive part of the Lennard-Jones potential. **a/d**) DFT predictions at an external potential of $\beta\mu = -3$. **b/e**) DFT predictions at an external potential of $\beta\mu = 0$. **c/f**) DFT predictions at an external potential of $\beta\mu = 3$.

solution for $\beta\mu = 3$, whereas $F_\theta^{(2)}$ provides a relatively accurate estimate (Fig. S.2f).

5. CONSTRUCTION OF EXTERNAL POTENTIALS

The inhomogeneous density profiles used in this work, both for performance evaluation and training of the neural functional $F_\theta^{(1)}$, were generated via MC simulations subjected to various external potentials. These external potentials consist of randomized variations of well-potentials and Gaussian potentials.

The form of the well-potentials is adapted from Cats *et al.* [2], where

$$\beta V_{\text{well}}(z) = \begin{cases} 0 & \text{for } |z| \in [-w\frac{L}{2}, w\frac{L}{2}], \\ s \left(\frac{|z| - w\frac{L}{2}}{(1-w)\frac{L}{2}} \right)^p & \text{for } |z| > w\frac{L}{2}. \end{cases} \quad (\text{S.14})$$

Here, s represents the dimensionless strength characterizing the potential at $|z| = L/2$, uniformly sampled with $s \sim \mathcal{U}(40, 60)$; w denotes the width of the central part of the slit ($\beta V_{\text{ext}} = 0$) and was uniformly sampled with $w \sim \mathcal{U}(0.4, 0.9)$; p characterizes the steepness of the potential and was uniformly sampled with $p \sim \mathcal{U}(2, 9)$.

The Gaussian potentials were constructed as a sum of

Gaussians, expressed as

$$\beta V_{\text{Gauss}}(z) = \sum_{i=1}^N h_i \exp\left(-\frac{(z - \mu_i)^2}{2\sigma_i^2}\right), \quad (\text{S.15})$$

where the number of Gaussians N is randomly chosen between $N = 0$ and $N = 10$; the mean of the Gaussians μ_i is uniformly sampled from $\mu \sim \mathcal{U}(0, L)$; the standard deviation of the Gaussians σ_i is uniformly sampled from $\sigma \sim \mathcal{U}(0, L/10) + L/100$; the height of the Gaussians h_i is randomly sampled from a squared normal distribution, $h \sim \mathcal{U}^2(\mu = 0, \sigma^2 = 1)$.

The potentials constructed from a combination of well-potentials and Gaussian potentials were simply constructed by summing the individual potentials

$$\beta V_{\text{ext}}(z) = \beta (V_{\text{well}}(z) + V_{\text{Gauss}}(z)). \quad (\text{S.16})$$

For the results shown in Fig. 2 of the main text, simulations were performed for 150 distinct external potentials, of which 50 densities were generated using pure well-potentials, 50 were generated using a set of Gaussian potentials and 50 were generated using a combination of well-potentials and Gaussian potentials.

To train the neural functional $F_\theta^{(1)}$, a distinct dataset was constructed by using 200 pure well-potentials; 500 Gaussian potentials; 300 combinations of well-potentials

and Gaussian potentials; 100 systems without an external potential. All simulations were conducted at a randomly selected chemical potential $\beta\mu \in [-4, 0.5]$.

6. OBTAINING THE EXCESS FREE ENERGY FROM SIMULATION

The excess Helmholtz free energy of the homogeneous bulk fluid (at a fixed volume V and temperature T) can be obtained from grand-canonical simulation via the equilibrium grand potential $\Omega_{eq}(\mu)$. The latter can be obtained by thermodynamic integration

$$\Omega_{eq}(\mu) = - \int_{-\infty}^{\mu} d\mu' N(\mu'), \quad (\text{S.17})$$

where $N(\mu') = V\rho_b(\mu')$ is the simulated (average) number of particles at chemical potential μ' in this homogeneous bulk system. Using the thermodynamic relation $\Omega_{eq} = \mathcal{F} - \mu N$ and $\mathcal{F} = \mathcal{F}_{id} + \mathcal{F}_{exc}$ with $\mathcal{F}_{id} = Nk_B T(\ln(N\Lambda^3/V) - 1)$, we arrive at $\mathcal{F}_{exc} = \Omega_{eq} + \mu(N)N - \mathcal{F}_{id}$. Here $\mu(N)$ is the inverse of $N(\mu)$, and we can identify \mathcal{F}_{exc} with the excess free-energy functional evaluated at the homogeneous bulk, $\mathcal{F}_{exc}[\rho_b]$.

To calculate the integral of Eq. (S.17), we sample the number of particles for a system in steps of $\Delta\beta\mu = 0.2$, for a range of $\beta\mu = -4$ (corresponding to a bulk density of $\rho_b\sigma^3 = 0.02$) up to the target chemical potential. The resulting excess free energy from simulations is favorably compared with its neural-network representations $F_{\theta}^{(1)}$ and $F_{\theta}^{(2)}$ in Fig. 2 of the main text.

7. NUMERICAL ERRORS IN THE RADIAL DISTRIBUTION FUNCTION

The derivation of $g(r)$ from $c^{(2)}(z)$ involves several extensive transformations, which can introduce sensitivity to numerical errors. This numerical instability is most pronounced when $g(r) \rightarrow 0$, as shown in Fig. S.3.

To reduce the numerical errors in this region, we employ a filter defined as follows

$$g_{\text{filter}}(r_i) = \begin{cases} 0 & \text{for all } r_i < r_0, \\ g(r_i) & \text{otherwise,} \end{cases} \quad (\text{S.18})$$

where r_0 is the highest r_i for which $g(r_i) \leq 0$.

8. SAMPLING IN PLANAR GEOMETRY SYSTEMS VS. ARBITRARY 3D SYSTEMS

The density profiles in planar geometry used in this study require approximately 1 hour of CPU time per density profile. Extrapolating these times naively to full three-dimensional density profiles, it would require an

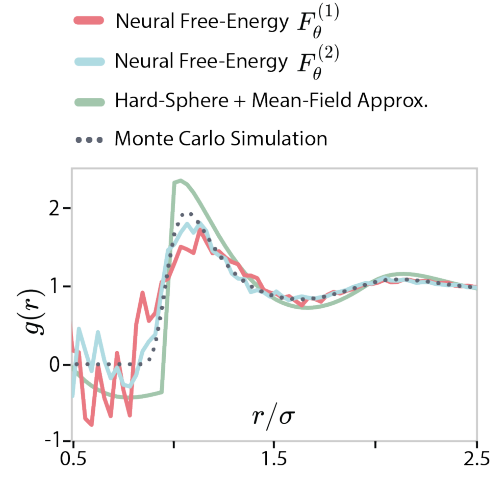


FIG. S.3: Unfiltered estimates of the radial distribution function for $\rho_b\sigma^3 = 0.62$. The radial distribution estimates from the neural functionals $F_{\theta}^{(1)}$, $F_{\theta}^{(2)}$ and F_{exc}^{MF} , which represents the analytical approximation of the White-Bear mark II version of Fundamental Measure Theory (FMT) combined with a mean-field approximation for the attractive part of the Lennard-Jones potential, are compared with simulation results.

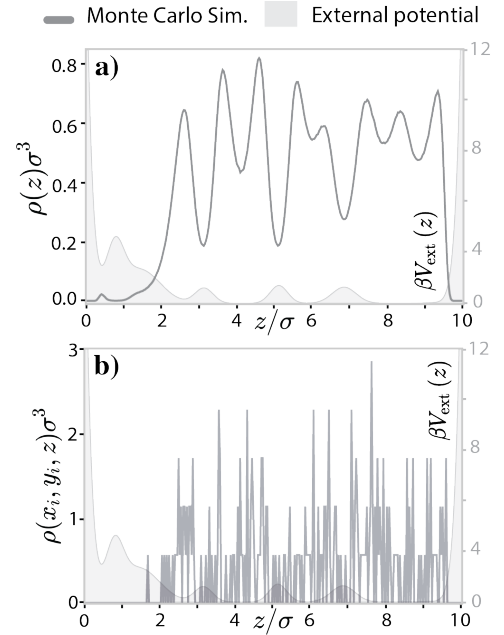


FIG. S.4: Comparison between sampling densities $\rho(z)$ in planar geometry and $\rho(x, y, z)$ in arbitrary three-dimensional geometry. **a)** $\rho(z)$ in an external potential $V_{\text{ext}}(z)$ (shown in gray) sampled from a MC simulation with 10^9 trial moves **b)** Slice of $\rho(x, y, z)$ at x_i for the same laterally symmetric external potential $V_{\text{ext}}(z)$, also sampled from a MC simulation with 10^9 trial moves.

impractical $A/(\Delta x \Delta y) \cdot 1 \text{ hours} = 102400 \text{ hours}$ to generate each density with similar accuracy for a resolution of $\Delta x = \Delta y = \Delta z = \sigma/32$ as used in this work. To illustrate this, we compare a 1D slice from a 3D density profile with a 1D density profile in planar geometry, both sampled within the same number of MC steps (10^9 trial moves with 10^7 equilibration moves and 4 decorrelation cycles) (Fig. S.4). These density profiles are constructed by binning particle positions in intervals of $4 \cdot N_{\text{particles}}$ trial moves throughout the MC simulation. After completion of the simulation, only a very low number of particles has been counted in each bin of the 3D histogram that constructs the density of Fig. S.4b. Many bins remain empty and many contain only a few particles, creating the discrete peaks of Fig. S.4b.

This illustrates that much longer sampling times are necessary to sample accurate three-dimensional density profiles. The results presented in this paper provide a compelling alternative: the radial distribution functions

sampled for this work were already obtained from 3D bulk systems, after which they were numerically transformed into direct correlation functions in planar geometry. This means that it is likely that the same dataset of radial distribution functions can be used when extending this approach to arbitrarily three-dimensional systems, with the only difference that a numerical transformation to the *radially symmetric* pair-correlation function $c^{(2)}(r)$ needs to be applied.

-
- [1] R. Evans, The nature of the liquid-vapour interface and other topics in the statistical mechanics of non-uniform, classical fluids, *Adv. Phys.* **28**, 143 (1979).
 - [2] P. Cats, S. Kuipers, S. De Wind, R. Van Damme, G. M. Coli, M. Dijkstra, and R. Van Roij, Machine-learning free-energy functionals using density profiles from simulations, *APL Mater.* **9**, 10.1063/5.0042558 (2021), arxiv:2101.01942.